DRAFT VERSION JANUARY 21, 2009
Preprint typeset using LATEX style emulateapj v. 05/04/06

arXiv:0901.2177v1 [astro-ph.EP] 15 Jan 2009

MODELING POROUS DUST GRAINS WITH BALLISTIC AGGREGATES. II. LIGHT SCATTERING PROPERTIES

YUE SHEN, B. T. DRAINE, AND ERIC T. JOHNSON
Princeton University Observatory, Princeton, NJ 08544

Draft version January 21, 2009

ABSTRACT

We study the light scattering properties of random ballistic aggregates constructed in Shen et al. (Paper I). Using the discrete-dipole-approximation, we compute the scattering phase function and linear polarization for random aggregates with various sizes and porosities, and with two different compositions: 100% silicate and 50% silicate-50% graphite. We investigate the dependence of light scattering properties on wavelength, cluster size and porosity using these aggregate models. We find that while the shape of the phase function depends mainly on the size parameter of the aggregates, the linear polarization depends on both the size parameter and the porosity of the aggregates, with increasing degree of polarization as the porosity increases. Contrary to previous studies, we argue that monomer size has negligible effects on the light scattering properties of ballistic aggregates, as long as the constituent monomer is smaller than the incident wavelength up to $2\pi a_0/\lambda \sim 1.6$ where a_0 is the monomer radius. Previous claims for such monomer size effects are in fact the combined effects of size parameter and porosity. Finally, we present aggregate models that can reproduce the phase function and polarization of scattered light from the AU Mic debris disk and from cometary dust, including the negative polarization observed for comets at scattering angles $160° \lesssim \theta < 180°$. These aggregates have moderate porosities, $\mathcal{P} \approx 0.6$, and are of sub-μm-size for the debris disk case, or μm-size for the comet case.

Subject headings: dust, extinction – polarization – scattering – circumstellar matter – comets – interplanetary medium – stars: individual (AU Mic, GJ 803)

1. INTRODUCTION

Interplanetary dust particles (IDPs) collected in the Earth's stratosphere by high-flying aircraft (Brownlee 1985; Warren et al. 1994) usually have irregular shapes and fluffy structures. Similar structures have been produced in laboratory and microgravity experiments of dust particle interactions (Wurm & Blum 1998; Blum & Wurm 2000; Krause & Blum 2004). It has also been suggested that interstellar dust grains may consist primarily of such aggregate structures (e.g., Mathis & Whiffen 1989; Dorschner & Henning 1995), with a mixture of various chemical compositions and vacuum.

Porous, composite aggregates are often modeled as a cluster of small spheres ("spherules" or "monomers"), assembled under various aggregation rules. The optical properties of these aggregates can be calculated using numerical schemes such as the generalized multisphere Mie (GMM) solution (Mackowski 1991; Xu 1997) or the discrete dipole approximation (DDA) method (e.g., Purcell & Pennypacker 1973; Draine & Flatau 1994). These methods have been used to study the optical properties of different kinds of aggregates during the past decade (e.g., West 1991; Lumme & Rahola 1994; Petrova et al. 2000; Kimura et al. 2006; Bertini et al. 2007; Lasue et al. 2009); most of those studies are dedicated to interpret the phase function and polarization of light scattered by cometary dust.

In a companion paper (Shen et al. 2008, hereafter Paper I), we constructed aggregates using three specific aggregation rules: ballistic agglomeration (BA), ballistic agglomeration with one migration (BAM1) and ballistic agglomeration with two migrations (BAM2). We developed a set of parameters to characterize the irregular structure of these aggregates. While the BA clusters are essentially the Ballistic Particle-Cluster Agglomeration (BPCA) clusters frequently used in the literature (e.g., West 1991; Kozasa et al. 1992, 1993; Ossenkopf 1993; Kimura et al. 2006; Bertini et al. 2007; Lasue et al. 2009), the newly-introduced BAM1 and BAM2 clusters have geometries that are random but substantially less "fluffy" than the BA clusters. The effective porosity $\mathcal{P}$ (eq. 12 in Paper I) increases from BAM2→BAM1→BA and covers a wide dynamical range, allowing us to investigate the effects of porosity on the optical properties of the aggregates in a systematic way. Using these aggregation rules, we can construct grain models with various sizes and compositions. In Paper I, we computed total scattering and absorption cross sections for the three types of aggregates (BA, BAM1 and BAM2), for three different compositions (50% silicate and 50% graphite; 50% silicate and 50% amorphous carbon AC1, Rouleau & Martin 1991, and 100% silicate), and for wavelengths from 0.1 μm to 4 μm. The purpose of this paper is to investigate the detailed light scattering properties of these aggregates, i.e., the phase function and the linear polarization.

The paper is organized as follows: in §2 we recapitulate our aggregate models; the scattering phase function and linear polarization for various ballistic aggregates are presented in §3, where we explore the dependence of light scattering properties on aggregate properties; we present examples of aggregates that can be applied to circumstellar debris disks and cometary dust in §4, and we show that moderate porosity aggregates can reproduce the observed scattering and polarization properties of dust in both solar system comets and extrasolar debris disks. We summarize our results in §5.

2. AGGREGATE MODELS

A detailed description of the target generation algorithms and resulting geometric properties of the BA, BAM1 and BAM2 clusters can be found in Paper I. Here we review some of the basic concepts that will be used in the following sections.

TABLE 1
CLUSTER GEOMETRIES

cluster	$\mathcal{P}$	$R/a_{\rm eff}$	$N_{\rm dip}$	$n_{\rm dip}$	Figs.
BA.256.1	0.8598	1.9249	115656	451.8	6
BA.256.2	0.8525	1.8925	105855	413.5	6
BA.256.3	0.8553	1.9050	102725	401.3	6
BAM1.32.4	0.6188	1.3791	13903	434.5	4ab
BAM1.256.1	0.7060	1.5038	103921	405.9	6
BAM1.256.2	0.7412	1.5693	107160	418.6	6
BAM1.256.3	0.6980	1.4904	107047	418.2	6
BAM2.256.1	0.5632	1.3179	113696	444.1	1,3,4cd,5,6,7
BAM2.256.2	0.5781	1.3333	103509	404.3	1,3,4cd,5,6,7
BAM2.256.3	0.5818	1.3372	107332	419.3	1,3,4cd,5,6,7
BAM2.512.14	0.6127	1.3719	211211	412.5	4ab
BAM2.1024.1	0.6386	1.4039	414977	405.3	4cd,8
BAM2.1024.2	0.6476	1.4158	412077	402.4	4cd,8
BAM2.1024.3	0.6387	1.4041	430184	420.1	4cd,8

NOTE. — Naming convention: "BA.256.1" means realization 1 of the N = 256 BA clusters.

Each aggregate is composed of N spherical monomers with radius a_0. We define the "effective radius" of a cluster, $a_{\rm eff}$, to be the radius of an equal-volume solid sphere; thus our aggregates have

$$a_{\rm eff} = N^{1/3} a_0 \ . \qquad (1)$$

The structure of the cluster is characterized by a porosity parameter $\mathcal{P}$ (see eq. 12 of Paper I) and a characteristic radius $R \equiv a_{\rm eff}/(1-\mathcal{P})^{1/3}$ (see eq. 11 of Paper I), which depends on $\mathcal{P}$ and is typically $1-2$ times $a_{\rm eff}$. Tables 1 and 2 of Paper I give tabulated mean values of $\mathcal{P}$ and $R/a_{\rm eff}$ for the three types of aggregates with $2^3 \leq N \leq 2^{16}$. For a given value of N, the BA clusters have the highest $\mathcal{P}$, while the BAM2 clusters have the lowest $\mathcal{P}$. Information for the specific cluster geometries employed in this paper can be found in Table 1, including the porosity $\mathcal{P}$, the number $N_{\rm dip}$ of dipoles representing the realization, and the number of dipoles per sphere, $n_{\rm dip} = N_{\rm dip}/N$. The actual geometry (including images) of these and other realizations of BA, BAM1, and BAM2 clusters can be obtained online.[1]

In Paper I we considered three different compositions: 50% silicate + 50% graphite, 50% silicate + 50% AC1, and 100% silicate. Silicate material accounts for perhaps 2/3 of the total mass of interstellar dust, and it is natural to assume that silicates will also provide the bulk of the refractory material in comets or debris disks. Interstellar silicates are amorphous; and amorphous silicates are believed to dominate the silicate mass even in the case of comets or circumstellar disks where crystalline silicates have been detected. We use the "astrosilicate" dielectric function (Draine & Lee 1984; Draine 2003).

Carbonaceous material provides a significant fraction of the total mass of interstellar grains, and this may also be true of dust in comets and debris disks. The smallest carbonaceous particles in the ISM consist primarily of polycyclic aromatic hydrocarbon material, but the form of the carbon in the larger grains (where most of the carbon resides) remains uncertain: Pendleton & Allamandola (2002) conclude that the hydrocarbon material is $\sim$ 85% aromatic (ring-like) and 15% aliphatic (chain-like), but Dartois et al. (2004) claim that aliphatic material predominates, with at most 15% of the carbon in aromatic form. To explore the effect of material that is strongly absorptive in the visible, we use the dielectric tensor of graphite for the carbon in our mixed-composition aggregates.

In the present paper we study the scattering properties of aggregates with two compositions: 100% silicate, or 50% silicate + 50% graphite (volume fractions). In Paper I we found that aggregates consisting of 50% silicate + 50% AC1 amorphous carbon had scattering properties intermediate between the 100% silicate and 50% silicate + 50% graphite aggregates.

Calculations are performed using DDSCAT version 7.0 (Draine & Flatau 2008). DDSCAT is a code based on the discrete dipole approximation (Purcell & Pennypacker 1973; Draine & Flatau 1994), designed to compute scattering and absorption of electromagnetic waves by targets with arbitrary geometry and composition, for targets that are not too large compared to the wavelength λ. For each cluster type (defined by N, aggregation rule, and composition) we generally average over three random realizations and 54 orientations for each realization.[2] DDSCAT 7.0 allows us to treat the graphite monomers as randomly-oriented spheres with the anisotropic dielectric tensor of graphite.

3. SCATTERING PHASE FUNCTION AND POLARIZATION

The phase function and linear polarization of the scattered light as functions of scattering angle θ can be retrieved from the elements of the 4×4 Muller matrix S_{ij} (e.g., Bohren & Huffman 1983). For unpolarized incident light, the scattered light phase function is proportional to $S_{11} = (4\pi^2/\lambda^2) dC_{\rm sca}/d\Omega$ (where $dC_{\rm sca}/d\Omega$ is the differential scattering cross section for unpolarized incident light) and the linear polarization parameter is $p = -S_{21}/S_{11}$. By definition, the polarization is perpendicular/parallel to the scattering plane when p is positive/negative.

We have obtained $S_{11}(\theta)$ and $p(\theta)$ for our realization- and orientation-averaged aggregates for wavelengths $0.1 \leq \lambda/\mu{\rm m} \leq 4$. For illustrative purposes, in most cases we will present the results for the BAM2 aggregates – the aggregate geometry with the lowest porosity. Orientation-averaged scattering properties for the clusters studied in this paper (including wavelengths not shown in the figures) are available online.[3]

3.1. *Wavelength Dependence*

We first show the wavelength dependence of S_{11} and linear polarization for N = 256-monomer BAM2 clusters with monomer radius $a_0 = 0.02\,\mu$m in Figure 1, for selected wavelengths. For the N = 256 BAM2 case, $a_{\rm eff} = 0.127\ \mu$m, the porosity $\mathcal{P} \approx 0.58$ (see Table 1), and the characteristic radius $R \approx 1.334 a_{\rm eff} = 0.17\,\mu$m . The phase function shows a relatively smooth dependence on wavelength λ: for $\lambda \lesssim 0.5\,\mu$m ($x \equiv 2\pi R/\lambda > 2$), it shows a strong peak in the forward scattering and a mild backscattering enhancement, with the overall forward-backward asymmetry decreasing monotonically as the incident wavelength increases. For linear polarization, the situation is more complicated. The polarization near $\theta \approx 90^\circ$ first decreases as λ increases, reaches a minimum at $\lambda \approx R$, and then rises again with increasing λ, approaching $p(90^\circ)$ = 100% in the Rayleigh limit. The wavelength $\lambda_{\rm min.pol}$ where $p(90^\circ)$ is minimum is well-defined for the pure silicate, with $\lambda_{\rm min.pol} \approx 0.17\,\mu$m. For the graphite-silicate composition it is less well-defined, with minima near $\sim 0.17\,\mu$m and $\sim 0.45\,\mu$m. The increase of polarization with increasing wavelength in the optical band is known as the polarization color effect in cometary scattered light observations (e.g., Chernova et al. 1996; Levasseur-Regourd & Hadancik 2001). The reverse behavior of increasing polarization with decreasing wavelength in the UV band, however, is more complicated to interpret. It could be caused by the change in the size parameter $x \equiv 2\pi R/\lambda$, or changes in the dielectric function as λ varies, or both. We will return to this point in §3.3.

---

[1] http://www.astro.princeton.edu/∼draine/agglom.html

[2] 9 values of the angle Θ between the cluster principal axis $\hat{\bf a}_1$ and $\hat{\bf x}$ (the direction of the incident light), and 6 values of the rotation angle β of the cluster around $\hat{\bf a}_1$. We use a single value of the rotation angle Φ of $\hat{\bf a}_1$ around $\hat{\bf x}$ because we average over 4 scattering planes.

[3] http://www.astro.princeton.edu/∼draine/SDJ09.html

It was shown in Paper I that the EMT-Mie model provides a good approximation for the total extinction cross section as a function of λ, provided that the vacuum fraction $f_{\rm vac}$ is set to $f_{\rm vac} \approx \mathcal{P}$. We now test to see if the EMT-Mie model reproduces the scattering phase function $S_{11}(\theta)$ and polarization $p(\theta)$. For the EMT-Mie calculations we use an optimal value of vacuum fraction $f_{\rm vac} = 0.55$ and the same amount of solid material as in the $N = 256$ BAM2 clusters. For the effective dielectric permittivity $\epsilon_{\rm eff}$ we use the Bruggeman rule (see Bohren & Huffman 1983)

$$\sum_i f_i \frac{\epsilon_i - \epsilon_{\rm eff}}{\epsilon_i + 2\epsilon_{\rm eff}} = 0 \ , \qquad (2)$$

where f_i and ϵ_i are the volume fraction and dielectric permittivity of each composition, including vacuum. There is always only one solution of $\epsilon_{\rm eff}$ that is physically meaningful. For graphite, we make the usual $\frac{1}{3}-\frac{2}{3}$ approximation, and take $\epsilon = \epsilon(E \parallel c)$ for $f = \frac{1}{3} f_{\rm graphite}$, $\epsilon = \epsilon(E \perp c)$ for $f = \frac{2}{3} f_{\rm graphite}$.

The EMT-Mie results are shown in Fig. 2 for the silicate-graphite and the pure silicate cases, in parallel to Fig. 1. The EMT calculations at fixed wavelength show resonances that arise from the use of spheres, but these should be smoothed out when modeling nonspherical particles, which are randomly-oriented and will not show such well-defined resonances. Therefore we have smoothed the EMT results using a Gaussian kernel

$$\bar{S}_{ij} = \frac{\int d\ln a \exp\left[-\left[\ln(a/\bar{a})\right]^2/2\sigma^2\right] S_{ij}(a)}{\int d\ln a \exp\left[-\left[\ln(a/\bar{a})\right]^2/2\sigma^2\right]} \qquad (3)$$

where $\sigma = \bar{a}/(\bar{a}+\lambda/2\pi)$ and $\bar{a} = (1-f_{\rm vac})^{-1/3} a_{\rm eff}$ is the radius of the Mie sphere. The phase function and polarization are then computed using the smoothed $\bar{S}_{ij}$.

By directly comparing Fig. 1 and Fig. 2 it is evident that the EMT-Mie results for $S_{11}(\theta)$ and linear polarization $p(\theta)$ do share the same trends we see in the DDA calculations. Nevertheless, there are substantial differences between the EMT-Mie results and our DDA results. One obvious feature is that the EMT-Mie model tends to underestimate the backscattering for short wavelength ($\lambda \lesssim 0.6\ \mu$m, $x \gtrsim 1.8$), a feature already revealed by the behavior of the asymmetry parameter $g \equiv \langle\cos\theta\rangle$ discussed in Paper I (fig. 12). For example, consider the forward-backward asymmetry $S_{11}(0)/S_{11}(180^\circ)$ for $\lambda = 0.168\,\mu$m: the DDA calculations for the mixed graphite-silicate BAM2 cluster give ~ 450, while the EMT-Mie calculation gives ~ 7000.

To compare the EMT-Mie results and our DDA calculations in detail we plot the relative differences in Fig. 3, for the silicate plus graphite case (upper) and the pure silicate case (bottom). The difference can be substantial for specific wavelengths or scattering angles. For example, for $\theta \approx 90^\circ$ scattering at $\lambda \approx 0.50\,\mu$m, the EMT-Mie calculation underestimates the polarization by a factor ~ 2, for both the graphite-silicate clusters and the pure silicate clusters. Although Paper I showed that EMT-Mie calculations can be used to obtain moderately accurate total extinction and scattering cross sections, Figure 3 shows that the scattering phase function and polarization estimated using EMT-Mie calculations do not accurately reproduce the scattering properties of irregular clusters.

3.2. *Does Monomer Size Matter?*

There is another parameter that might affect S_{11} and polarization: the monomer size. There have been claims that large monomer size is crucial in decreasing the polarization and in producing the negative polarization branch observed in cometary dust (e.g., Petrova et al. 2000; Bertini et al. 2007). However, in these previous studies, variations of monomer size were always coupled with changes in porosity $\mathcal{P}$ and cluster size R, hence effects attributed to varying the monomer size may in fact be due to variations in $\mathcal{P}$ or R. We have already seen in Paper I that the apparent effects of monomer size on total cross sections are essentially the effects of varying $\mathcal{P}$ or R.

To isolate the effect of monomer size, we compare clusters with the same $a_{\rm eff}$ and very similar $\mathcal{P}$ (thus R is also comparable), but different monomer size a_0. Thus the effect of monomer size, if there is any, is decoupled from other effects. We first consider the same example used in figure 8 of Paper I: the $N = 32$ BAM1 cluster realization BAM1.32.4 ($\mathcal{P} = 0.619$, $R/a_{\rm eff} = 1.379$) with monomer size $a_0 = 0.0504\,\mu$m and the $N = 512$ BAM2 cluster realization BAM2.512.14 ($\mathcal{P} = 0.613$, $R/a_{\rm eff} = 1.372$) with $a_0 = 0.02\,\mu$m. Both clusters have $a_{\rm eff} = 0.160\,\mu$m and $R = 0.220\,\mu$m. The orientation-averaged results are shown in Fig. 4a,b for two wavelengths and for the silicate-graphite composition only. Although there are slight differences, the two cases have similar phase functions and polarizations: at constant R and $\mathcal{P}$, varying the monomer size a_0 had little effect on the phase function and polarization.

The above example employed moderate-sized clusters ($x = 2\pi R/\lambda \lesssim 3.9$) composed of small monomers ($2\pi a_0/\lambda \lesssim 0.9$). Fig. 4c,d compares the scattering properties of 2 large clusters ($R \approx 1.4\,\mu$m, $x = 11.1$ and 13.9) with similar porosities $\mathcal{P} \approx 0.6$ but different monomer sizes. For $\lambda = 0.631\,\mu$m and $0.794\,\mu$m, clusters with $a_0 = 0.10\,\mu$m and $0.16\,\mu$m show similar (though not identical because of the slight difference in porosity of the two clusters; see §3.4) polarization $p(\theta)$, despite the substantial difference in monomer size.

3.3. *Dependence on Cluster Size*

As we have discussed in §3.1 for fixed-size clusters, the dependence of the phase function and linear polarization on wavelength λ is likely caused by the changes in both the size parameter and dielectric function. To investigate the effects of cluster size at fixed incident wavelength (i.e., the effects of size parameter alone), we use $N = 256$, BAM2 clusters with monomer size $a_0 = 0.02, 0.025, 0.03\,\mu$m, or $R \sim 0.169, 0.212, 0.254\,\mu$m. These clusters have the same porosity, and as argued in the previous section, monomer size has negligible effects, hence any difference must be caused by changes in R. The results are shown in Fig. 5 for both compositions. We present results at two wavelengths: $\lambda = 0.126\,\mu$m ($< R$) and $\lambda = 0.631\,\mu$m ($> R$). In both cases the backward/forward scattering asymmetry increases with increasing the size parameter $2\pi R/\lambda$.

In general, we expect $p(90^\circ) \to 1$ in the Rayleigh scattering limit $R/\lambda \ll 1$, with the peak polarization decreasing with increasing R/λ. This decline with increasing R/λ is seen in

Figure 5b,d. However, the results in Figure 5a,c show that the variation of $p_{\rm max}$ with increasing R is not monotonic: at $\lambda = 0.126\,\mu$m when $R \gtrsim \lambda$ and when the dielectric function is very absorptive, for both the 100% silicate and 50% silicate + 50% graphite $N = 256$ BAM2 clusters, the polarization is an increasing function of R over the range $1.3 \lesssim R/\lambda \lesssim 2$. Thus for these cases the polarization at $\lambda = 0.126\,\mu$m has a minimum at some size $R_{\rm crit} < 1.3\lambda$.

However, the dependence of polarization on R/λ depends on the dielectric function (and therefore on both composition and wavelength). For $\lambda = 0.631\,\mu$m the 100% silicate BAM2 clusters with $\mathcal{P} \approx 0.6$ have the polarization declining with increasing R out to $R/\lambda = 2.2$ (the largest value computed, see §4.2 and Figs. 7d and 8) – without showing a reversal in the polarization behavior. The situation is even more complicated for the silicate plus graphite case, where there is no coherent trend when $R \approx \lambda$ (see Figs. 1a, 7a and 7b). Based on the cases investigated thus far, it appears that when the dielectric function has only weak absorption (e.g., 100% astrosilicate at $\lambda = 0.631\,\mu$m), for fixed porosity $\mathcal{P}$ the polarization is a monotonically decreasing function of cluster size R from the Rayleigh limit $R \ll \lambda$ up to $R/\lambda \lesssim 2$. On the other hand, when the dielectric function is strongly absorptive (e.g., materials at $\lambda = 0.126\,\mu$m or silicate-graphite clusters at $\lambda = 0.631\,\mu$m), for fixed porosity the polarization declines with increasing R from the Rayleigh limit until it reaches a local minimum at $R \approx \lambda$ (the transition is less distinct for the silicate-graphite case than for the pure silicate case), and then rises as R is further increased, at least out to $R/\lambda \approx 2$ (e.g., Figs. 5a and 7a,b).

3.4. *Dependence on Porosity*

We now investigate the effect of porosity on the scattering phase function and linear polarization. Previous studies on the porosity effect using only the BPCA and/or the even more porous "ballistic cluster-cluster agglomeration (BCCA)" clusters were quite limited in the dynamical range of porosity, and changes in porosity were coupled with changes in cluster size. To decouple from the cluster size effect we choose clusters with comparable sizes, but different porosities. We use $N = 256$ BA, BAM1 and BAM2 clusters, with monomer size $a_0 = 143, 170, 200$ Å respectively; hence these clusters have comparable size $R \sim 0.17\,\mu$m, but different porosities $\mathcal{P} = 0.85, 0.74, 0.58$.

We consider two regimes: $\lambda < R$ and $\lambda > R$. The results are shown in Fig. 6 for two example wavelengths, $\lambda = 0.126\,\mu$m and $\lambda = 0.447\,\mu$m, and for the two compositions. It is evident that in both regimes, porosity has little effect on the shape of the phase function[4]. On the other hand, higher porosity tends to increase the linear polarization for both $R > \lambda$ and $R < \lambda$.

Most of the cases shown in this section have large linear polarization fraction [$p(90^\circ) \gtrsim 50\%$]. Cometary dust typically has $p(90^\circ) \lesssim 40\%$ and a negative branch of polarization at scattering angle $\sim 160^\circ - 180^\circ$ (e.g., Levasseur-Regourd & Hadancik 2001), observed at optical wavelengths. From the results of §3.1-§3.4 we expect that, in general, a reduced peak polarization and appearance of a negative polarization branch for $160 \lesssim \theta < 180^\circ$ can be obtained by (1) increasing the cluster size R and (2) making the cluster more compact (lower porosity $\mathcal{P}$). Examples of ballistic aggregates that are able to reproduce these cometary dust features will be presented in §4.2.

4. APPLICATIONS OF BALLISTIC AGGREGATES

The light scattering properties of our ballistic aggregates can be applied to various observations. Here we focus on debris disks and cometary dust, where single scattering dominates in the optically thin regime. We show examples of aggregates that can reproduce qualitative and quantitative features observed in the scattered light from the debris disk around AU Mic (Graham et al. 2007) and from cometary dust (e.g., Lumme & Rahola 1994; Petrova et al. 2000; Kimura et al. 2006; Lasue et al. 2009). Due to computational limits, we cannot probe a sufficiently large parameter space to claim that our models are unique; nor do we attempt to fit a sophisticated model to the observations of a specific comet. Nevertheless, our examples (in particular the moderate-porosity BAM2 clusters) nicely reproduce most of the features observed in light scattered by debris-disk dust and cometary dust.

4.1. *Debris disk around AU Mic*

Polarization maps of the debris disk surrounding the nearby M star AU Microscopii have been obtained by Graham et al. (2007) using *HST* ACS in the F606W optical band ($\lambda_c = 0.590\,\mu{\rm m}, \Delta\lambda = 0.230\,\mu$m). The scattered light is polarized perpendicular to the disk plane. Graham et al. (2007) adopted the form for the phase function introduced by Henyey & Greenstein (1940):

$$S_{11} = \frac{1}{4\pi}\frac{1-g^2}{(1+g^2-2g\cos\theta)^{3/2}} \quad , \tag{4}$$

assumed that the polarization vs. scattering angle varies as

$$p(\theta) = -\frac{S_{21}}{S_{11}} = p_{\rm max}\frac{\sin^2\theta}{1+\cos^2\theta} \quad , \tag{5}$$

and simultaneously fitted the phase function and linear polarization as function of scattering angle to the observational data, obtaining $g \approx 0.68$ and $p_{\rm max} \approx 0.53$. Graham et al. (2007) suggest that very porous ($\mathcal{P} \approx 0.91-0.94$) μm-sized spherical grains or aggregates can produce these features based on Mie theory and DDA calculations for BA clusters (Kimura et al. 2006).

Here we will show that random aggregates with a much lower porosity ($\mathcal{P} \approx 0.6$) can, in fact, better fit the observations of the AU Mic debris disk. To reproduce the observed features, we require that the phase function and linear polarization are both close to the functions (4) and (5) with the the best-fit values of g and $p_{\rm max}$ found by Graham et al. (2007). In particular, the intensity of scattered light at $\theta = 0^\circ$ should be approximately a factor of 150 larger than the intensity at $\theta = 180^\circ$, and the maximum polarization should be ≈ 0.5, although $p(\theta)$ need not necessarily peak at $\theta = 90^\circ$.

Dust grains in debris disks will have a distribution of sizes. Much of the interstellar grain mass can be approximated by a power-law size distribution $dn/dR \propto R^{-\alpha}$ for $R \lesssim 0.25\,\mu$m with $\alpha \approx 3.5$ (Mathis et al. 1977). Size distributions with $\alpha \approx 3.5$ can be obtained from models with coagulation and collisional fragmentation (Dohnanyi 1969; Tanaka et al. 1996; Weidenschilling 1997).

For modeling comets and debris disks, we will consider a size distribution $dn/dR \propto R^{-3.5}$. For a fixed porosity (i.e., a particular type of aggregate with a fixed N), this size distribution is just $dn/da_0 \propto a_0^{-3.5}$, where a_0 is the monomer size.

---

[4] The slight difference in $S_{11}/S_{11}(0)$ is likely caused by the different geometry of the BA, BAM1 and BAM2 clusters.

Hence the averaged phase function $S_{11}(\theta)$ and polarization are:

$$\bar{S}_{11}(\theta) = \frac{\int_{a_{\min}}^{a_{\max}} da_0 (dn/da_0) S_{11}(a_0,\theta)}{\int_{a_{\min}}^{a_{\max}} da_0 (dn/da_0)} , \tag{6}$$

$$\bar{p}(\theta) = \frac{\int_{a_{\min}}^{a_{\max}} da_0 (dn/da_0) S_{11}(a_0,\theta) p(a_0,\theta)}{\int_{a_{\min}}^{a_{\max}} da_0 (dn/da_0) S_{11}(a_0,\theta)} , \tag{7}$$

where $a_{\min}$ and $a_{\max}$ are the minimum and maximum values of monomer size in our size distribution.

We consider $N = 256$ BAM2 clusters ($\mathcal{P} = 0.58$), with $a_0 = 0.02, 0.03, 0.04, 0.05, 0.06, 0.07, 0.08\,\mu$m, which correspond to $R \approx 0.169, 0.254, 0.339, 0.424, 0.508, 0.593, 0.678\,\mu$m. We show the calculated phase function and polarization for each of these clusters (averaged over orientations and 3 realizations) in Fig. 7, at two wavelengths $\lambda = 0.501$ and $0.631\,\mu$m. For comparison with the scattering properties inferred for the dust around AU Mic, we calculate $\bar{S}_{11}(\theta)$ and polarization $\bar{p}(\theta)$ averaged over a size distribution $dn/dR \propto R^{-3.5}$ with $a_{\min} = 0.015\,\mu$m and $a_{\max} = 0.065\,\mu$m ($R_{\min} = 0.127\,\mu$m, $R_{\max} = 0.551\,\mu$m), which are shown as dashed lines. The best-fit Henyey-Greenstein phase function (4) and polarization fitting function (5) from Graham et al. (2007) are shown as solid black lines. We plot the comparison for both the silicate-graphite composition (upper panels) and the pure silicate composition (bottom panels).

As we can see from Fig. 7, the size-averaged silicate-graphite clusters produce close matches to the Henyey-Greenstein model at these optical wavelengths for both the phase function and linear polarization. These clusters have porosity $\mathcal{P} \approx 0.6$ and overall size $R \sim 0.2-0.5\,\mu$m, i.e., they are sub-μm-sized clusters with moderate porosity.

As discussed in §3.4, increasing porosity will increase the polarization of scattered light. Our highest-porosity clusters are those BA clusters, which are commonly used in the literature, referred to as "ballistic particle-cluster agglomeration (BPCA)" clusters (e.g., West 1991; Kozasa et al. 1992, 1993; Ossenkopf 1993; Kimura et al. 2006; Bertini et al. 2007; Lasue et al. 2009). We found that if we replace the BAM2 clusters in Fig. 7 with BA clusters with the same number of monomers and monomer sizes, we can reproduce similar phase function features but over-predict the polarization. This is already seen in Graham et al. (2007) (e.g., their fig. 8). Thus we conclude that compact BAM2 clusters fit the observations of AU Mic better than the more porous BA clusters that have been considered previously.

4.2. *Cometary Dust*

The phase function and linear polarization of scattered light have been observed in a variety of comets. Though different comets show quantitative differences in the phase function and polarization, there are some common features:

- The phase function shows strong forward scattering with a weak enhancement in the backscattering; the geometric albedo [defined as $A \equiv (S_{11}[180°]\lambda^2)/(4\pi G)$ where $G \approx \pi R^2$ is the averaged geometric cross section of the grain] of backscattered light is less than 0.06 (e.g., Hanner & Newburn 1989).

- The linear polarization $p(\theta)$ is a bell-shaped curve as function of scattering angle, with typical maximum value of $10-30\%$ (Dobrovolsky et al. 1986; Levasseur-Regourd et al. 1996), although gas contamination in polarimetric measurements with wide-band filters might depolarize the observed scattered light (Kiselev et al. 2004).

- Within the 4000–7000Å window, the polarization increases with wavelength, which is the so-called polarization color effect (e.g., Chernova et al. 1996; Levasseur-Regourd & Hadancik 2001).

- Many comets show a negative branch of polarization at scattering angle larger than $150-160°$, with a minimum of $\gtrsim -2\%$ (e.g., Dollfus et al. 1988; Eaton et al. 1992).

Most of these features, in particular the negative polarization branch, have been successfully reproduced using various aggregates which differ in geometry, composition and porosity (e.g., Lumme & Rahola 1994; Petrova et al. 2000; Kimura et al. 2006; Bertini et al. 2007; Lasue et al. 2009). The aggregates studied here are capable of producing all these features as well. In addition, we have demonstrated the effects of grain size and porosity, and pointed out that the monomer size effect claimed by previous authors is in fact due to changes in cluster size R and/or porosity $\mathcal{P}$. For example, in Petrova et al. (2000) and Bertini et al. (2007), the difference of the prominence of the negative branch is caused by the effect of grain size when they increase the monomer size for the same configuration/porosity.

The reason that those authors did not find a negative branch of polarization for small monomer size ($a_0 \lesssim 0.1\ \mu$m) and moderate number of monomers (a few tens) is that computational limits prevented them from using a sufficient number of monomers. To test this, we have computed a few realizations of BAM2 clusters with $N = 1024$, composed of small monomers ($a_0 = 0.08\ \mu$m). The results are shown in Fig. 8 for optical wavelength $\lambda = 0.631\ \mu$m, where the negative branch is evident for both compositions (it is more prominent at the usually observed red band $\lambda = 0.55\,\mu$m). In Fig. 8, we have also computed for the $N = 1024$ BAM2 clusters using monomer size $a_0 = 0.1\,\mu$m, shown as open squares; the dashed lines are the average of the results of the two monomer sizes, for a size distribution $dn/dR \propto R^{-3.5}$ running from $R_{\min} = 0.98\,\mu$m to $R_{\max} = 1.54\,\mu$m.

These clusters are μm-size grains, which is consistent with the values found by other authors (e.g., Lumme & Rahola 1994; Petrova et al. 2000; Kimura et al. 2006), although the exact values depend on composition as well as porosity. We find that the $N = 1024$, $a_0 = 0.08, 0.1\ \mu$m BAM2 clusters composed of silicate and graphite (Fig. 8a) with $R \approx 1.1-1.4\,\mu$m and $\mathcal{P} \approx 0.6$, reproduce a backscattering albedo $A = [S_{11}(180°)\lambda^2]/(4\pi^2 R^2) \sim 0.04$ and a small negative polarization for scattering angles $\sim 155-180°$ peaking at ($\sim -1\%$), representative of the typical values found in cometary observations, although the maximum polarization ($\sim 45\%$) is a little higher than observed. We may need somewhat more compact aggregates, or different composition (e.g., more silicate, see the right panel of Fig. 8) to lower the peak polarization. Alternatively, one may consider the mixture of fluffy aggregates and compact solid grains (e.g., Lasue et al. 2009). In their study, a larger fraction of porous BCCA aggregates is needed to produce a higher peak polarization for comet C/1995 O1 Hale-Bopp than for comet 1P/Halley, consistent with our argument that high porosity helps increase the polarization. Since only very porous BCCA clusters were used in their modeling, it will be interesting to see if our more compact BAM1 and BAM2 clusters will provide better fits for these comets in modeling the mixture of fluffy aggregates and compact solid grains.

5. CONCLUSIONS

We have studied the phase function and linear polarization properties of light scattering by ballistic aggregates. We studied the wavelength dependence, cluster size dependence, and porosity dependence of the light scattering properties using the discrete-dipole-approximation, and compared with the EMT-Mie model. Our main conclusions are:

1. It is shown that though the EMT-Mie model reproduces similar trends in these dependences, it differs quantitatively from the DDA calculations. We recommend using DDA calculations if accurate results are desired.

2. Monomer size has negligible effects on the scattered light properties as long as monomers are small compared with the incident wavelength λ. Even when the monomers are no longer small (e.g., $2\pi a_0/\lambda \sim 1.6$), monomer size appears to be of secondary importance for the phase function and polarization $p(\theta)$.

3. The phase function is mainly determined by R/λ; increasing R/λ decreases the backscattering relative to forward scattering.

4. When $R/\lambda \ll 1$ (e.g., in the Rayleigh limit), increasing R/λ decreases the polarization. For $R \gtrsim \lambda$, the dependence of polarization on R/λ depends on the dielectric function: for materials that are not strongly absorbing, increasing R/λ results in decreasing polarization, at least for $R/\lambda \lesssim 2$ (e.g., Figure 7c,d, showing 100% silicate BAM2 clusters at $\lambda = 0.501\,\mu$m and $0.631\,\mu$m); however, at vacuum UV wavelengths where the materials are strongly absorbing, increasing R/λ can increase the polarization (e.g., Figure 5a,c, showing scattering at $\lambda = 0.126\,\mu$m).

5. The degree of polarization depends on the size parameter as well as porosity, but high porosity helps increase polarization in both the $R \lesssim \lambda$ and $R \gtrsim \lambda$ regimes.

6. We present aggregates with BAM2 geometry, moderate porosity $\mathcal{P} \approx 0.6$, and sub-μm sizes which can reproduce the scattered light phase function and polarization observed in the AU Mic debris disk.

7. We present aggregate models with BAM2 geometry and moderate porosity $\mathcal{P} \approx 0.6$ that can reproduce the albedo and polarization $p(\theta)$ observed for cometary dust, including the negative polarization observed at scattering angles $160^\circ \lesssim \theta < 180^\circ$. These aggregates are composed of silicate and graphite, and are of $\gtrsim \mu$m size. Such moderately porous aggregates are promising candidates for cometary dust.

This research was supported in part by NSF grant AST 04-06883. Computations were performed on the Della and Artemis computer clusters at Princeton University.

REFERENCES

Bertini, I., Thomas, N., & Barbieri, C. 2007, A&A, 461, 351
Blum, J., & Wurm, G. 2000, Icarus, 143, 138
Bohren, C. F., & Huffman, D. R. 1983, Absorption and Scattering of Light by Small Particles (New York: Wiley)
Brownlee, D. E. 1985, Annual Review of Earth and Planetary Sciences, 13, 147
Chernova, G. P., Jockers, K., & Kiselev, N. N. 1996, Icarus, 121, 38
Dartois, E., Muñoz Caro, G. M., Deboffle, D., & d'Hendecourt, L. 2004, A&A, 423, L33
Dobrovolsky, O. V., Kiselev, N. N., & Chernova, G. P. 1986, Earth Moon and Planets, 34, 189
Dohnanyi, J. W. 1969, J. Geophys. Res., 74, 2531
Dollfus, A., Bastien, P., Le Borgne, J.-F., Levasseur-Regourd, A. C., & Mukai, T. 1988, A&A, 206, 348
Dorschner, J., & Henning, T. 1995, A&A Rev., 6, 271
Draine, B. T. 2003, ApJ, 598, 1017
Draine, B. T., & Flatau, P. 1994, J. Opt. Soc. Am. A , 11, 1491
—. 2008, http://arXiv.org/abs/astro-ph/0809.0337
Draine, B. T., & Lee, H. M. 1984, ApJ, 285, 89
Eaton, N., Scarrott, S. M., & Gledhill, T. M. 1992, MNRAS, 258, 384
Graham, J. R., Kalas, P. G., & Matthews, B. C. 2007, ApJ, 654, 595
Hanner, M. S., & Newburn, R. L. 1989, AJ, 97, 254
Henyey, L. G., & Greenstein, J. L. 1940, Annales d'Astrophysique, 3, 117
Kimura, H., Kolokolova, L., & Mann, I. 2006, A&A, 449, 1243
Kiselev, N. N., Jockers, K., & Bonev, T. 2004, Icarus, 168, 385
Kozasa, T., Blum, J., & Mukai, T. 1992, A&A, 263, 423
Kozasa, T., Blum, J., Okamoto, H., & Mukai, T. 1993, A&A, 276, 278
Krause, M., & Blum, J. 2004, Phys. Rev. Lett., 93, 021103
Lasue, J., Levasseur-Regourd, A. C., Hadamcik, E., & Alcouffe, G. 2009, Icarus, 199, 129
Levasseur-Regourd, A. C., Hadamcik, E., & Renard, J. B. 1996, A&A, 313, 327
Levasseur-Regourd, A. C., & Hadancik, E. 2001, in ESA SP-495: Meteoroids 2001 Conference, ed. B. Warmbein, 587–594
Lumme, K., & Rahola, J. 1994, ApJ, 425, 653
Mackowski, D. W. 1991, Proc. Royal Soc. London Ser A, 433, 599
Mathis, J. S., Rumpl, W., & Nordsieck, K. H. 1977, ApJ, 217, 425
Mathis, J. S., & Whiffen, G. 1989, ApJ, 341, 808
Ossenkopf, V. 1993, A&A, 280, 617
Pendleton, Y. J., & Allamandola, L. J. 2002, ApJS, 138, 75
Petrova, E. V., Jockers, K., & Kiselev, N. N. 2000, Icarus, 148, 526
Purcell, E. M., & Pennypacker, C. R. 1973, ApJ, 186, 705
Rouleau, F., & Martin, P. G. 1991, ApJ, 377, 526
Shen, Y., Draine, B. T., & Johnson, E. T. 2008, ApJ, 689, 260
Tanaka, H., Inaba, S., & Nakazawa, K. 1996, Icarus, 123, 450
Warren, J. L., Barrett, R. A., Dodson, A. L., Watts, L. A., & Zolensky, M. E. 1994, Cosmic Dust Catalog, 14
Weidenschilling, S. J. 1997, Icarus, 127, 290
West, R. A. 1991, Appl. Opt., 30, 5316
Wurm, G., & Blum, J. 1998, Icarus, 132, 125
Xu, Y.-L. 1997, Appl. Opt., 36, 9496

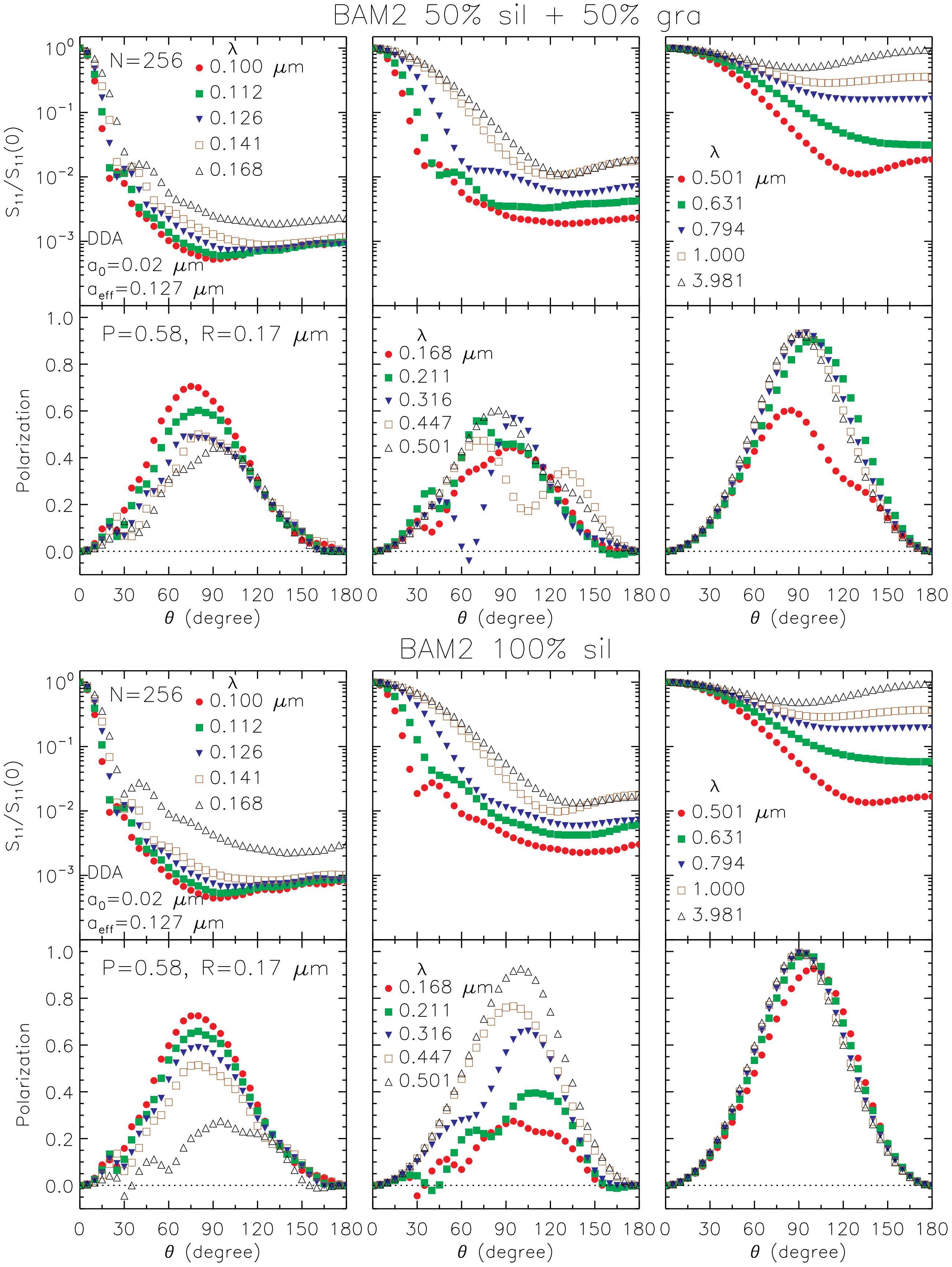

FIG. 1.— Wavelength dependence of S_{11} [normalized using $S_{11}(0)$] and polarization for the $N = 256$ and $a_0 = 0.02$ μm BAM2 clusters for two compositions, averaged over 3 realizations (BAM2.256.1-3) and 54 random orientations for each realization. *Upper*: the silicate-graphite case; *bottom*: the 100% silicate case.

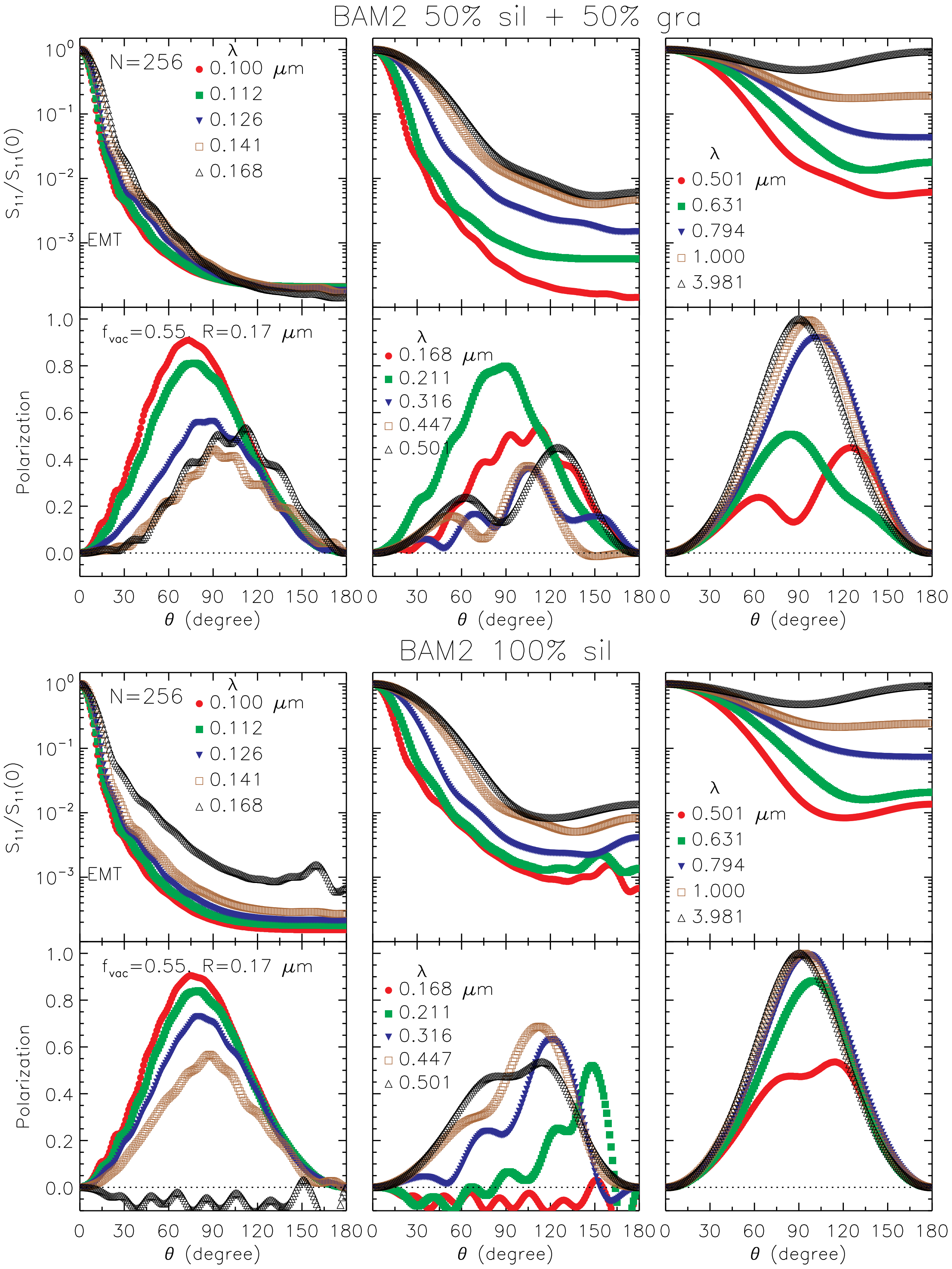

FIG. 2.— Same as Fig. 1, but for the EMT-Mie results (smoothed as in eq. 3) computed for $f_{\rm vac}$ = 0.55 and same amount of solid material as in the N = 256 BAM2 clusters in Fig. 1.

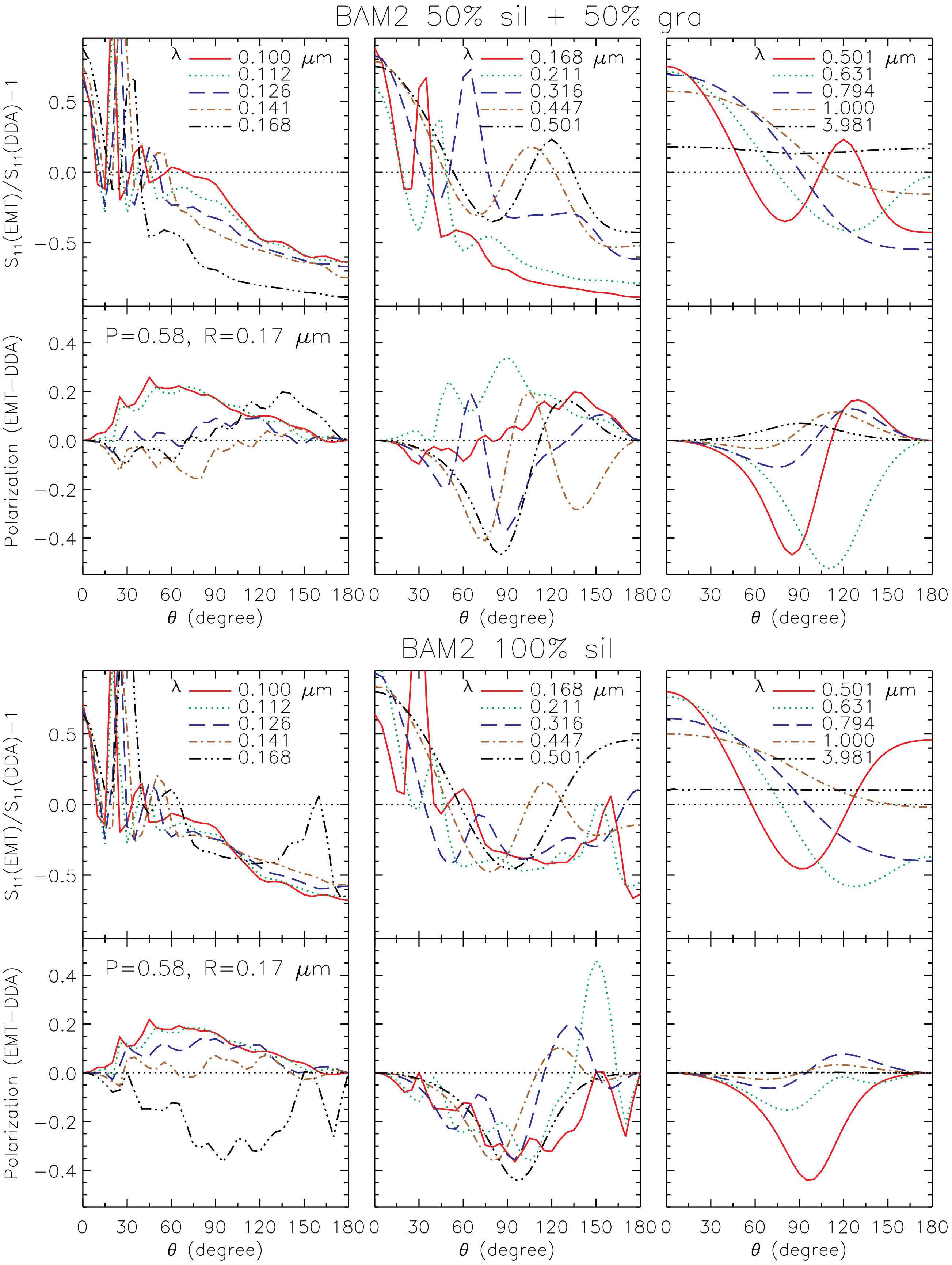

FIG. 3.— Difference in the phase function and polarization for the DDA results for the $N = 256$ BAM2 clusters from Fig. 1 and EMT results from Fig. 2.

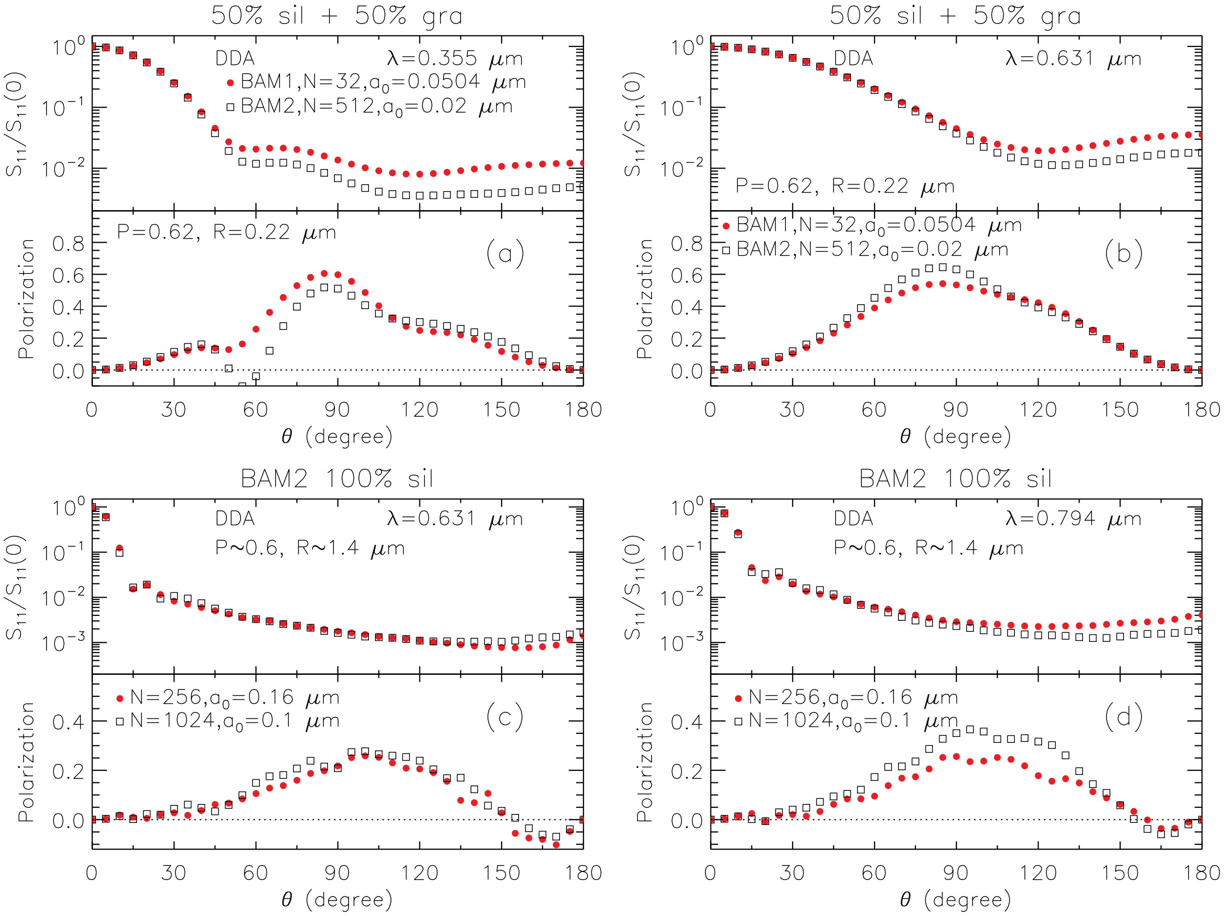

FIG. 4.— Tests for the effect of monomer size. (a) Comparable phase function and polarization for two silicate-graphite clusters – BAM1.32.4 and BAM2.512.14 – with similar porosities $\mathcal{P} \sim 0.619, 0.613$ and cluster size $R \sim 0.221, 0.220\,\mu$m, but different monomer size $a_0 = 0.0504, 0.02\,\mu$m, for $\lambda = 0.355\,\mu$m ($x \equiv 2\pi R/\lambda = 3.9$). (b) Same as (a), but for $\lambda = 0.631\,\mu$m ($x = 2.2$). (c) Comparable phase function and polarization at $\lambda = 0.631\,\mu$m for two large silicate clusters with similar porosity $\mathcal{P} \sim 0.57$ and 0.64, and size $R \sim 1.4\,\mu$m ($x = 13.9$), but different monomer size $a_0 = 0.10, 0.16\,\mu$m ($2\pi a_0/\lambda = 1.0, 1.6$). (d) Same as (c), but for $\lambda = 0.794\,\mu$m. The clusters in (c) and (d) are each represented by 3 realizations (BAM2.256.1-3 and BAM2.1024.1-3) and 54 orientations per realization. These four examples show that for fixed size R and porosity $\mathcal{P}$, the monomer size a_0 is unimportant if $2\pi a_0/\lambda < 1$, and of only secondary importance even when $2\pi a_0/\lambda \approx 2$.

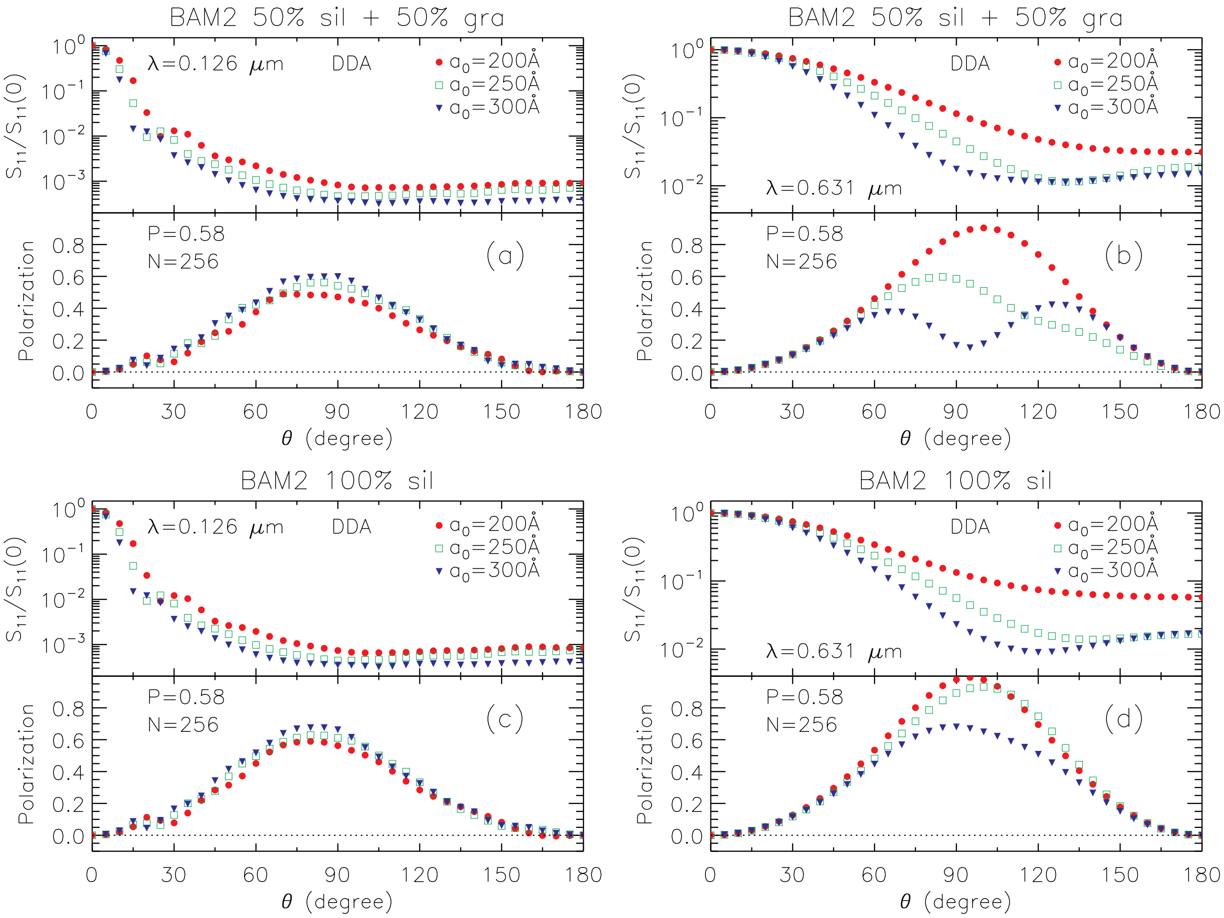

FIG. 5.— Cluster size dependence of S_{11} and polarization for $N = 256$ BAM2 clusters with $a_0 = 0.02, 0.025, 0.03\,\mu$m, for two compositions, averaged over 3 realizations (BAM2.256.1-3) and 54 random orientations. These clusters have typical sizes $R \sim 0.169$, 0.212, 0.254 μm, but same porosity $\mathcal{P} \sim 0.58$. Examples are shown at incident wavelength $\lambda = 0.126\,\mu$m $< R$ and 0.631 μm $> R$.

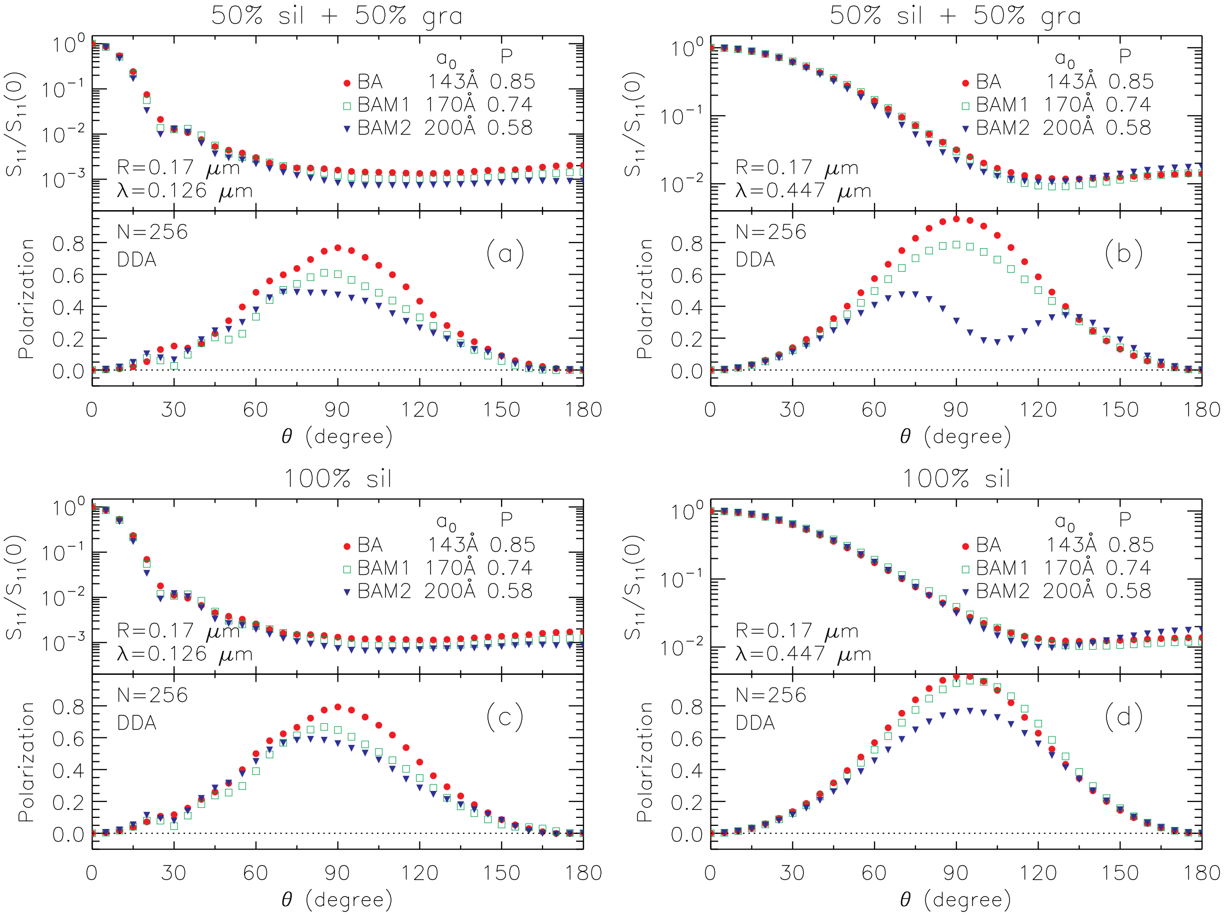

FIG. 6.— Effect of porosity on S_{11} and polarization for N = 256 BA, BAM1 and BAM2 clusters which have the same cluster size $R \sim 0.17\,\mu$m but different porosities $\mathcal{P}$ = 0.85, 0.74, 0.58, using three realizations per cluster (BA.256.1-3, BAM1.256.1-3, and BAM2.256.1-3) and 54 orientations per realization.

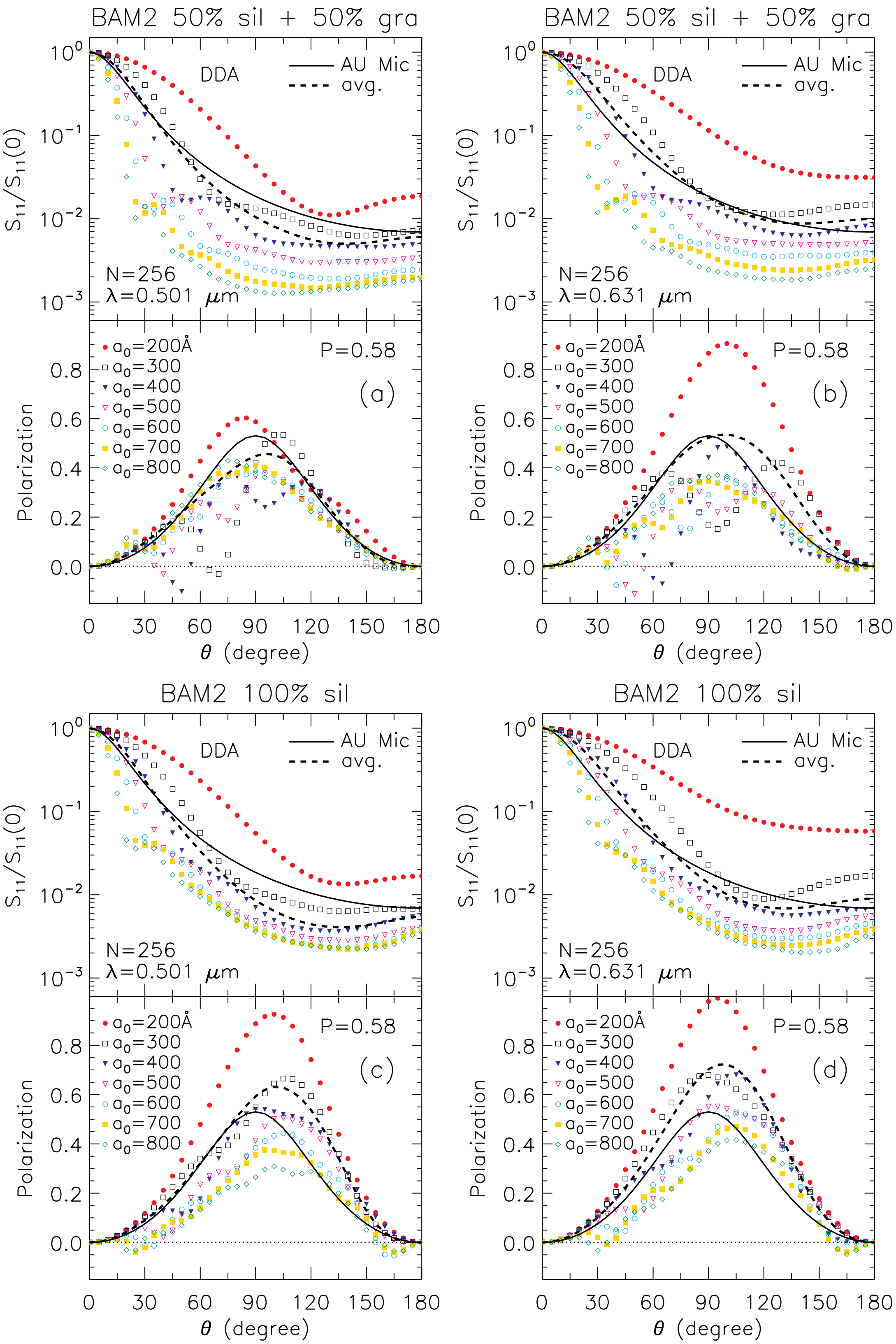

FIG. 7.— Applications to the debris disk around AU Mic. Scattering properties $S_{11}(\theta)/S_{11}(0)$ and $p(\theta)$ for 3 realizations of $N = 256$ BAM2 clusters (BAM2.256.1-3), 54 orientations per realization, with monomer sizes a_0 ranging from 200Å to 800Å (R from 0.169μm to 0.678μm). Dashed lines show scattering properties obtained by averaging over a size distribution $dn/dR \propto R^{-3.5}$ running from $R_{\rm min} = 0.127\,\mu$m to $R_{\rm max} = 0.551\mu$m (see text). Solid curves show phase function and polarization inferred by Graham et al. (2007) for an assumed angular dependence given by eq. (4,5). The adopted size distribution provides a good fit using clusters with porosity $\mathcal{P} \approx 0.6$ and sizes $R \approx 0.13-0.55\,\mu$m. For comparison, we also show results for clusters with $a_0 = 700, 800$ Å, which exhibit the negative polarization branch observed in comets. Scattering properties available at http://www.astro.princeton.edu/∼draine/SDJ09.html .

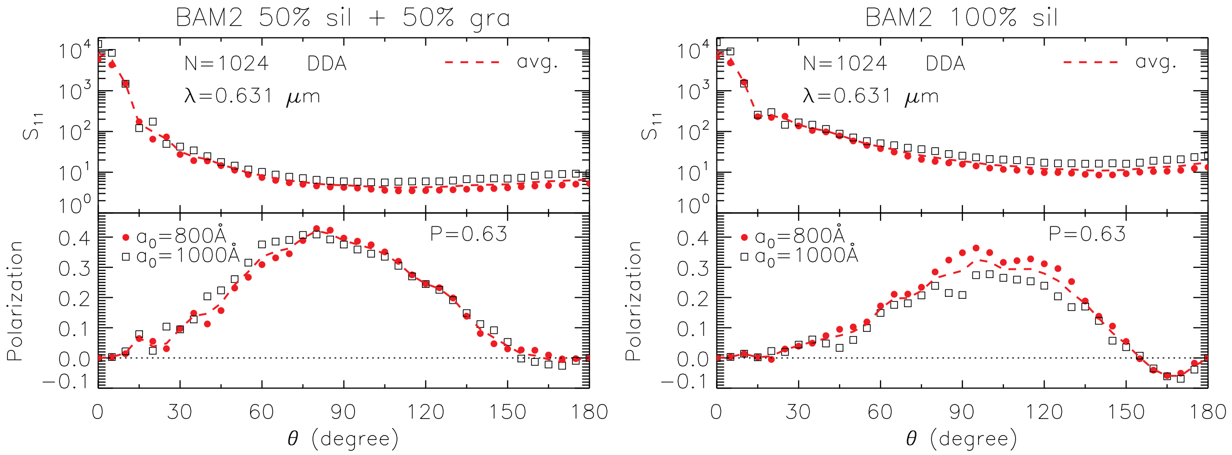

FIG. 8.— Scattering properties for aggregates resembling cometary dust (see text). For each composition we present results for $N = 1024$ BAM2 clusters (3 realizations, BAM2.1024.1-3, 54 orientations per realization) with monomer sizes $a_0 = 0.08$ and $0.1\,\mu$m ($R = 1.12\,\mu$m and $1.40\,\mu$m). Dashed lines are for a size distribution $dn/dR \propto R^{-3.5}$ for $0.98\,\mu\mathrm{m} < R < 1.54\,\mu$m. Scattering properties available at http://www.astro.princeton.edu/∼draine/SDJ09.html .